The Astrophysical Journal, 890:7 (14pp), 2020 February 10 https://doi.org/10.3847/1538-4357/ab61fd

Large-scale Structures in the CANDELS Fields: The Role of the Environment in Star Formation Activity

Nima Chartab[1], Bahram Mobasher[1], Behnam Darvish[2], Steve Finkelstein[3], Yicheng Guo[4], Dritan Kodra[5], Kyoung-Soo Lee[6], Jeffrey A. Newman[5], Camilla Pacifici[7], Casey Papovich[8], Zahra Sattari[1], Abtin Shahidi[1], Mark E. Dickinson[9], Sandra M. Faber[10], Henry C. Ferguson[7], Mauro Giavalisco[11], and Marziye Jafariyazani[1]
[1] Department of Physics and Astronomy, University of California, Riverside, 900 University Ave, Riverside, CA 92521, USA; nima.chartab@email.ucr.edu
[2] Cahill Center for Astrophysics, California Institute of Technology, 1216 East California Boulevard, Pasadena, CA 91125, USA
[3] Department of Astronomy, The University of Texas at Austin, Austin, TX 78712, USA
[4] Department of Physics and Astronomy, University of Missouri, Columbia, MO 65211, USA
[5] Department of Physics and Astronomy and PITT PACC, University of Pittsburgh, Pittsburgh, PA 15260, USA
[6] Department of Physics, Purdue University, 525 Northwestern Avenue, West Lafayette, IN 47907, USA
[7] Space Telescope Science Institute, 3700 San Martin Drive, Baltimore, MD 21218, USA
[8] Department of Physics and Astronomy, Texas A&M University, College Station, TX 77843-4242, USA
[9] National Optical Astronomy Observatories, 950 N. Cherry Avenue, Tucson, AZ 85719, USA
[10] University of California Observatories/Lick Observatory, University of California, Santa Cruz, CA 95064, USA
[11] Department of Astronomy, University of Massachusetts, 710 North Pleasant Street, Amherst, MA 01003, USA
Received 2019 October 15; revised 2019 December 2; accepted 2019 December 9; published 2020 February 6

Abstract

We present a robust method, weighted von Mises kernel density estimation, along with boundary correction to reconstruct the underlying number density field of galaxies. We apply this method to galaxies brighter than *Hubble Space Telescope*/F160w $\leqslant$ 26 AB mag in the redshift range $0.4 \leqslant z \leqslant 5$ in the five CANDELS fields (GOODS-N, GOODS-S, EGS, UDS, and COSMOS). We then use these measurements to explore the environmental dependence of the star formation activity of galaxies. We find strong evidence of environmental quenching for massive galaxies ($M \gtrsim 10^{11}\,M_{\odot}$) out to $z \sim 3.5$ such that an overdense environment hosts $\gtrsim$20% more massive quiescent galaxies than an underdense region. We also find that environmental quenching efficiency grows with stellar mass and reaches ~60% for massive galaxies at $z \sim 0.5$. The environmental quenching is also more efficient than stellar mass quenching for low-mass galaxies ($M \lesssim 10^{10}\,M_{\odot}$) at low and intermediate redshifts ($z \lesssim 1.2$). Our findings concur thoroughly with the "overconsumption" quenching model where the termination of cool gas accretion (cosmological starvation) happens in an overdense environment and the galaxy starts to consume its remaining gas reservoir in depletion time. The depletion time depends on the stellar mass and could explain the evolution of environmental quenching efficiency with stellar mass.

Unified Astronomy Thesaurus concepts: Galaxy environments (2029); Galaxy evolution (594); Large-scale structure of the universe (902); Galaxy quenching (2040)

Supporting material: animation, machine-readable table

1. Introduction

It is now well established that the observed properties of galaxies are correlated with their host environment. In the local universe, the environmental dependence of galaxy morphology and star formation rate (SFR) confirms that early-type passive galaxies often reside in dense environments, such as galaxy groups and clusters, whereas late-type and star-forming systems are mostly found in less dense environments, the so-called field (e.g., Dressler 1980; Balogh et al. 2004; Kauffmann et al. 2004; Peng et al. 2010; Woo et al. 2013). However, the situation is not entirely settled at intermediate to high redshifts. While there is convincing evidence for a density–morphology relation at intermediate redshifts (e.g., Capak et al. 2007), the exact trend in the density–SFR relation remains controversial. Some studies show a reverse relation so that on average the SFR is higher in a dense environment (Elbaz et al. 2007; Cooper et al. 2008), others find no significant correlation (Grützbauch et al. 2011; Scoville et al. 2013; Darvish et al. 2016), and some observe the same relation as in the local universe (Patel et al. 2009). Recently, an increasing number of studies have found that locally observed environmental quenching persists at least out to $z \sim 2$ (e.g., Fossati et al. 2017; Guo et al. 2017; Kawinwanichakij et al. 2017; Ji et al. 2018). Therefore, a comprehensive study is needed to ascertain the role of the environment in the star formation activity of galaxies at high redshifts.

Accurate measurement of the environment of galaxies is needed before any such study can be performed. One can use a variety of density estimators to quantify the environment in which galaxies are located. Darvish et al. (2015) have reviewed and compared different density estimators, including adaptive weighted kernel smoothing, 10th and 5th nearest neighbors, count-in-cell, weighted Voronoi tessellation, and Delaunay triangulation. Comparing with simulations, they found that the weighted kernel smoothing method is more reliable than the widely-used nearest neighbor and count-in-cell methods. Although kernel density estimation is a powerful and reliable technique for estimating the density field of galaxies, there are considerable ambiguities in the selection of the appropriate kernel function and optimized kernel window size (bandwidth). The selection of the bandwidth is the most crucial step in kernel density estimation. Small bandwidth results in an under-smoothed estimator, with high variability. On the other hand, large bandwidth causes an oversmoothed (biased) estimator. The boundary problem is another common issue regardless of

the density estimator, and the net effect is an underestimation of density near the boundaries since galaxies beyond the edge of the survey are missed. In this paper, we develop a new technique, weighted von Mises kernel density estimation considering boundary correction, to reconstruct the density field of galaxies.

While measurement of density enhancement is available in contiguous wide-area surveys such as the Cosmic Evolution Survey (COSMOS; Scoville et al. 2007), studying the influence of the environment on the evolution of low-mass galaxies ($M \lesssim 10^{10}\,M_{\odot}$) requires deep surveys that are often performed over much smaller areas because of the trade-off between the area coverage and the depth in galaxy surveys. The Cosmic Assembly Near-IR Deep Extragalactic Legacy Survey (CANDELS; Grogin et al. 2011; Koekemoer et al. 2011) includes extensive data in five fields, ideal for any study of the evolution of galaxies with redshift. The CANDELS provides: (1) multi-waveband deep data from the *Hubble Space Telescope* (*HST*) and *Spitzer Space Telescope* for all the five fields; (2) accurate measurement of the photometric redshifts, stellar mass, and SFRs with their probability distributions; (3) extensive spectroscopic observations for galaxies; (4) constraints on the cosmic variance using five widely separated fields. These make the CANDELS fields ideal for such studies. The challenge, however, is to perform a reliable estimate of the density measurements for such fields with limited volume.

In this paper, we make a publicly available catalog of density measurements for 86,716 galaxies brighter than F160w $\leqslant 26$ AB mag at $0.4 \leqslant z \leqslant 5$ in all the five CANDELS fields using weighted von Mises kernel density estimation, taking into account the boundary effect. We use a grid search cross-validation method to optimize the bandwidth of the kernel function. In order to reduce the projection effect, we use the full photo-z probability distribution function (PDF) of individual galaxies (D. Kodra et al. 2019, in preparation).

The paper is organized as follows. In Section 2, we discuss the data and describe the spectral energy distribution (SED) fitting procedure to measure the physical properties of galaxies. Section 3 describes our methodology for measuring the local environment of galaxies and presents the galaxy environment catalog and large-scale structure maps. In Section 4, we explore the role of the environment in the star formation activity of galaxies. We discuss our results in Section 5 and summarize them in Section 6.

Throughout this work, we assume a flat ΛCDM cosmology with $H_0 = 100\,h\,\mathrm{km\ s^{-1}\,Mpc^{-1}}$, $\Omega_{m_0} = 0.3$, and $\Omega_{\Lambda_0} = 0.7$. All magnitudes are expressed in the AB system and the physical parameters are measured assuming a Chabrier initial mass function.

2. Data

We use the *HST*/F160w (*H*-band) selected catalogs of the five CANDELS fields covering a total area of ∼960 arcmin^2: GOODS-S (Guo et al. 2013), GOODS-N (Barro et al. 2019), COSMOS (Nayyeri et al. 2017), EGS (Stefanon et al. 2017), and UDS (Galametz et al. 2013). The comoving coverage area of each field as a function of redshift is shown in Figure 1.

The catalogs are a combination of CANDELS wide, deep, and Hubble Ultra-Deep Field (HUDF) regions. The point-source 5σ limiting AB magnitude ranges from ∼27.4 to ∼29.7 in the wide and HUDF areas, respectively. However, the 5σ limiting magnitude is brighter for extended objects and depends on the surface brightness profile of sources. The limiting magnitude in the wide field reaches $H_{\rm lim} \sim 26$, which corresponds to 50% completeness at the median size of sources (Guo et al. 2013).

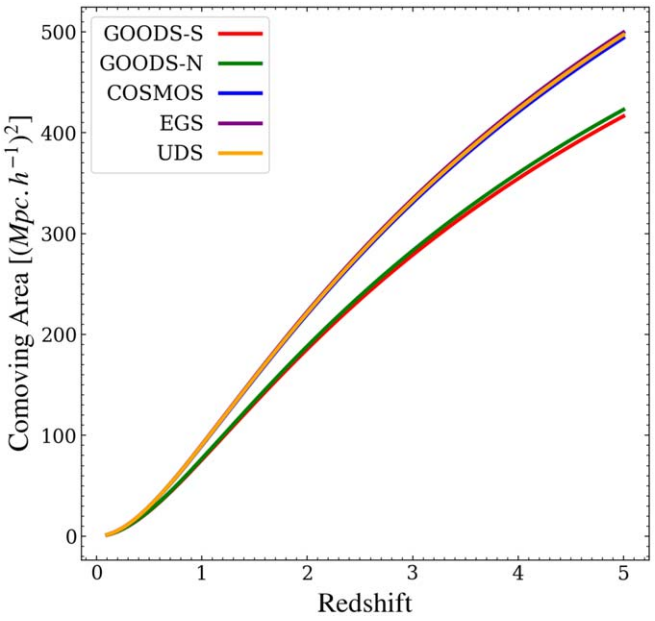

Figure 1. The comoving areal cover of the fields as a function of redshift. Each field covers a comoving area of $\sim 25\,h^{-2}\,\mathrm{Mpc}^2$ at $z \sim 0.5$ up to $\sim 450\,h^{-2}\,\mathrm{Mpc}^2$ at $z \sim 5$.

We utilize the updated CANDELS photometric redshift catalog (D. Kodra et al. 2019, in preparation), which provides accurate photometric redshifts with normalized median absolute deviation ($\sigma_{\rm NMAD}$) of ∼0.02, combined with the spectroscopic/3D-*HST* grism redshifts ($z_{\rm best}$). The catalog also contains redshift PDFs of galaxies determined by the minimum Frechet distance method. The Frechet distance (Alt & Godau 1995) is a measure of similarity between two curves (e.g., two measurements of photo-z PDFs). The best PDF is obtained based on the minimum of the Frechet distance among six independent z-PDF measurements.

In this work, we measure the local number density for a total of 86,716 galaxies selected based on the following criteria (Table 1):

1. Removing the stars by requiring SExtractor's stellarity parameter CLASS_STAR < 0.95.
2. Covering a redshift range $0.4 \leqslant z \leqslant 5$. We select galaxies with greater than 95% probability of being in this redshift range. We limit our analysis to $z \geqslant 0.4$ due to the small volume of the survey at lower redshifts.
3. A cut on *H*-band magnitude to remove sources fainter than 26 AB mag. Although the fields have different 5σ limiting magnitudes, we use a similar magnitude cut to have homogeneous and comparable samples.

2.1. Stellar Mass and SFRs

We perform SED fitting to derive physical parameters of galaxies such as stellar mass and SFR. We use the LePhare code (Arnouts et al. 1999; Ilbert et al. 2006) combined with a library of synthetic spectra generated by the population synthesis code of Bruzual & Charlot (2003). To perform SED fitting, we fix redshifts on $z_{\rm best}$ from the updated version of the CANDELS photometric redshift catalog. We assume an

Table 1
Summary of the Data Used in This Work

Field	Reference	Area (arcmin^2)	5σ Depth (AB)	All Objects	Final Sample[a]	Spec./grism z[b]
GOODS-S	Guo et al. (2013)	170	27.36	34,930	14,200	16%
GOODS-N	Barro et al. (2019)	170	27.8	35,445	15,746	18%
COSMOS	Nayyeri et al. (2017)	216	27.56	38,671	18,896	7%
EGS	Stefanon et al. (2017)	206	27.6	41,457	19,670	13%
UDS	Galametz et al. (2013)	202	27.45	35,932	18,204	7%

Notes.
[a] Criteria: (1) CLASS_STAR < 0.9, (2) probability of being in $0.4 \leqslant z \leqslant 5$ greater than 95%, (3) $H \leqslant 26$ AB mag.
[b] The percentage of galaxies in the final sample with confirmed spectroscopic/grism redshifts.

exponentially declining star formation history with nine e-folding times in the range 0.01 Gyr $< \tau <$ 30 Gyr. We adopt the initial mass function of Chabrier (2003), truncated at 0.1 and 100 $M_\odot$, and the attenuation law of Calzetti et al. (2000) to apply dust extinction ($E(B-V) \leqslant 1.1$). The code also includes emission lines using the relation of Kennicutt (1998) between SFR and UV luminosity, as described in Ilbert et al. (2009). Three different stellar metallicities are considered: $Z = 0.02$, 0.008, and 0.004.

The LePhare code computes fluxes in all given bands for each template, then finds the template with minimum χ^2 based on the model and observed fluxes. The best values of the physical parameters come from the template with the minimum χ^2. The code also provides the median of the stellar mass (M), SFR, and specific SFR (sSFR = SFR/M) along with uncertainties obtained from the marginalized probability distribution (probability $\propto e^{-\chi^2/2}$) of each parameter. In this work, we use the median values for stellar mass, SFR, and sSFR. We also obtain U, V, and J rest-frame colors from best-fit SEDs.

Figure 2 shows the distribution of stellar mass as a function of redshift for galaxies in the five fields. The stellar mass completeness limit (95%) associated with $H_{\rm lim} = 26$ is determined using the method introduced by Pozzetti et al. (2010). We divide the sample into redshift bins, separately in the case of all and quiescent populations. We utilize rest-frame U, V, and J colors along with the criteria of Muzzin et al. (2013) to select quiescent galaxies at $z < 4$. Beyond this redshift, we use an sSFR cut derived from the first quartile (<25th percentile) of the sSFR distribution to build a subsample of passive galaxies. We then measure the limiting stellar mass, $M_{\rm lim}$, for galaxies in the subsample, defined as the stellar mass that a galaxy would have if it had a magnitude equal to the adopted magnitude limit of the survey ($H_{\rm lim}$). If we consider a constant mass-to-light ratio, then $M_{\rm lim}$ for a galaxy with stellar mass M can be computed as $\log M_{\rm lim} = \log M + 0.4(H - H_{\rm lim})$. The stellar mass completeness limit ($M_{\rm min}(z)$) is the 95th percentile of the $M_{\rm lim}$ distribution for the 20% faintest sources in each redshift bin. Thus, if we take a sample of galaxies with stellar mass greater than the completeness limit, less than 5% of galaxies will be missed from the sample. As shown in Figure 2, the stellar mass completeness limit is higher for passive galaxies with higher mass-to-light ratios. Hence, we adopt the completeness limit derived from passive galaxies, which can be modeled with a quadratic polynomial: $\log(M_{\rm min}(z)/M_\odot) = 7.90 + z - 0.09z^2$.

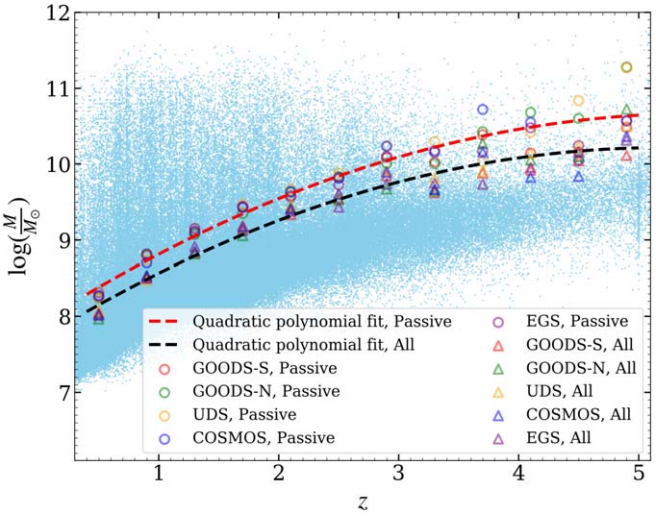

Figure 2. The stellar mass of galaxies as a function of their redshifts. The red (black) dashed line represents the 95% stellar mass completeness limit ($H_{\rm lim} = 26$) for the passive galaxies (all galaxies), determined using the method of Pozzetti et al. (2010).

3. Measuring Galaxy Environment

The environment of a galaxy is defined as the density field where that galaxy resides. To reconstruct the density field, we consider narrow redshift intervals (z-slices) and treat each z-slice as a two-dimensional structure. Using kernel density estimation, we calculate the density field within each z-slice. The location of a galaxy with photo-z is probabilistic and best identified by its redshift PDF. Thus, a galaxy with photometric redshift contributes to all z-slices. The contribution of each galaxy to different redshift intervals is proportional to the area under the photo-z PDF that lies within that interval. This introduces the weighted approach for density estimation. The density field associated with each galaxy is derived from the weighted sum of surface densities at different z-slices using the full redshift PDF of the galaxy. Therefore, the surface density, σ, of a galaxy at any given coordinate (R.A., decl.) is

$$\sigma_{(\rm R.A.,\,decl.)} = \sum_j \omega_j \sigma^j_{(\rm R.A.,\,decl.)} \quad (1)$$

where $\sigma^j_{(\rm R.A.,\,decl.)}$ is the surface number density field at the position (R.A., decl.) in the jth z-slice and ω_j is the probability of the desired galaxy being in the jth z-slice. Although $\sim$12% of our sample have spectroscopic/grism redshift, we do not use them to determine ω_j. This assures that our method is not biased in favor of galaxies with accurate spectroscopic/grism redshifts. Therefore, we rely on uniformly calculated photometric redshifts, with well-calibrated probability distributions (D. Kodra et al. 2019, in preparation) in ω_j estimation. We use the area underneath

the photometric redshift PDFs to obtain the likelihood of a galaxy being in the jth z-slice.

In order to measure $\sigma^j_{(\mathrm{R.A.,decl.})}$, we use the weighted von Mises kernel density estimation technique corrected for the boundary effect. In the following sections, we describe different steps for estimating σ^j: an estimate of the redshift bin size (Section 3.1), weighted von Mises kernel density estimation (Section 3.2), bandwidth selection of the kernel function (Section 3.3), and boundary correction (Section 3.4).

3.1. Selection of Redshift Slices

It is important to optimize the width of redshift slices to account for the extended structures. While the redshift of a galaxy can be used to measure its location along the line of sight, the estimate can be affected by redshift space distortion (RSD) due to the peculiar velocity of galaxies. The RSD effect is dependent on cosmological model such that a galaxy cluster with internal velocity dispersion Δv will be extended in comoving space ($\Delta\chi$) as

$$\Delta\chi = \frac{\Delta v}{H_0}\frac{1+z}{\sqrt{\Omega_{m_0}(1+z)^3 + \Omega_{\Lambda_0}}} \tag{2}$$

where H_0, Ω_{m_0}, and Ω_{Λ_0} are the present values of Hubble constant, matter density, and dark energy density respectively. Hence, what we observe is the combination of the density and the velocity field. The proper binning in redshift space to reconstruct 2D maps of the large-scale structures is constrained by both the typical size of a galaxy cluster in redshift space and redshift uncertainties. In the presence of less accurate photometric redshifts, we have two options, either using a weighted scheme to incorporate the contribution of each galaxy in all z-slices accurately or adopting wide z-slices to collect all signals from galaxies with large redshift uncertainties. Here we use the weighted approach such that the width of a z-slice is constrained based on the resolution of photo-z PDFs, $\Delta z/(1+z) \sim 1\%$ (D. Kodra et al. 2019, in preparation). This allows us to avoid oversmoothing caused by interlopers.

The comoving size of a galaxy cluster due to the RSD effect (Equation (2)) peaks at $z = (2\Omega_{\Lambda_0}/\Omega_{m_0})^{1/3} - 1 \simeq 0.65$. At that redshift, a massive galaxy cluster ($\Delta v \sim 1500\,\mathrm{km\,s^{-1}}$) will be extended $\sim 18\ h^{-1}$ Mpc in comoving space due to the peculiar velocity of its galaxies. In addition, the estimated redshift uncertainty ($\Delta z/(1+z) \sim 1\%$) limits the z-slice width to $35\,h^{-1}\,\mathrm{Mpc}$ ($\Delta v \sim 3000\ \mathrm{km\,s^{-1}}$). Therefore, we fix the width of redshift bins (at all redshifts) to a constant comoving size of $35\,h^{-1}\,\mathrm{Mpc}$ to satisfy both the RSD effect and the constraint on redshift uncertainty. This results in a total of 124 z-slices spanning from $z = 0.4$ to 5. One should note that the constant comoving width does not imply a constant redshift interval. For comparison, the width of a z-slice is 0.014 for $z = 0.4$, and 0.096 for $z = 5$.

3.2. Weighted von Mises Kernel Density Estimation

The distribution of galaxies in each z-slice is analogous to a two-dimensional map where galaxies are labeled with their weights ω_j, computed from the photometric redshift PDFs. These weights are assigned by determining the fraction of redshift PDF within each z-slice. A powerful non-parametric method for density estimation is weighted kernel density estimation (wKDE) (Parzen 1962), which can be written as

$$\sigma^j(\boldsymbol{X}_0) = \sum_i \widetilde{\omega}_i^j \mathrm{K}(\boldsymbol{X}_i;\, \boldsymbol{X}_0) \tag{3}$$

where $\sigma^j(\boldsymbol{X}_0)$ is the estimated density at the position $\boldsymbol{X}_0$ on the jth z-slice and K is the kernel function. The summation is over all data points ($\boldsymbol{X}_i$) that exist in the desired z-slice. $\widetilde{\omega}_i^j$ is the normalized weight associated with ith data point, in the jth z-slice so that $\sum_i \widetilde{\omega}_i^j = 1$.

An appropriate choice of the kernel function for spherical data (R.A., decl.) is the von Mises kernel (García-Portugués et al. 2013) expressed as

$$\mathrm{K}(\boldsymbol{X}_i;\, \boldsymbol{X}_0) = \frac{1}{4\pi b^2 \sinh(1/b^2)} \exp\left(\frac{\cos\psi}{b^2}\right) \tag{4}$$

where b is the global bandwidth of the kernel function, which is the main parameter in the wKDE method and controls the smoothness of the estimate. We will explain the bandwidth selection method in Section 3.3. ψ is the angular distance between $\boldsymbol{X}_i = (\mathrm{R.A.}_i,\ \mathrm{decl.}_i)$ and $\boldsymbol{X}_0 = (\mathrm{R.A.}_0,\ \mathrm{decl.}_0)$. $\cos\psi$ can be expressed as $\sin\mathrm{decl.}_i \sin\mathrm{decl.}_0 + \cos\mathrm{decl.}_i \cos\mathrm{decl.}_0 \cos(\mathrm{R.A.}_i - \mathrm{R.A.}_0)$.

It should be noted that a Gaussian kernel function cannot be used in the case of spherical data. The kernel function must integrate to unity and a Gaussian function does not satisfy this requirement on the spherical space.

3.3. Bandwidth Selection

Bandwidth selection is a challenging problem in kernel density estimation. Choosing too narrow a bandwidth leads to a high-variance estimate (undersmoothing), while too wide a bandwidth leads to a high-bias estimate (oversmoothing). This bias–variance tradeoff can be solved by maximizing the likelihood cross-validation (LCV) (Hall 1982), which is defined by

$$\mathrm{LCV}(b) = \frac{1}{N}\sum_{k=1}^{N} \log \sigma_{-k}(\boldsymbol{X}_k) \tag{5}$$

where N is the total number of data points in a given z-slice and $\sigma_{-k}(\boldsymbol{X}_k)$ is the kernel estimator computed at position $\boldsymbol{X}_k$ excluding the kth data point. We perform a grid search in the range from $0.^\circ0001$ to $0.^\circ03$ with 50 steps to find the optimized global bandwidth where LCV(b) is maximized. Figure 3 shows the LCV maximization results for one of the z-slices ($1.068 \leqslant z \leqslant 1.089$) in all CANDELS fields. For instance, the cross-validation method suggests $b = 0.^\circ0061$ (a comoving distance of 0.26 $h^{-1}\,\mathrm{Mpc}$) as the best bandwidth for the GOODS-S field at the mentioned z-slice. Figure 4 shows the optimized bandwidth in comoving coordinates for 124 redshift slices spanning from 0.4 to 5.

A constant bandwidth (b) over each z-slice may result in undersmoothing in regions with sparse observations and oversmoothing in crowded areas. By varying the bandwidth for each data point (i) and defining a local bandwidth (b_i), we reduce the bias in dense regions and the variance in regions with sparse data. To incorporate adaptive smoothing, we vary

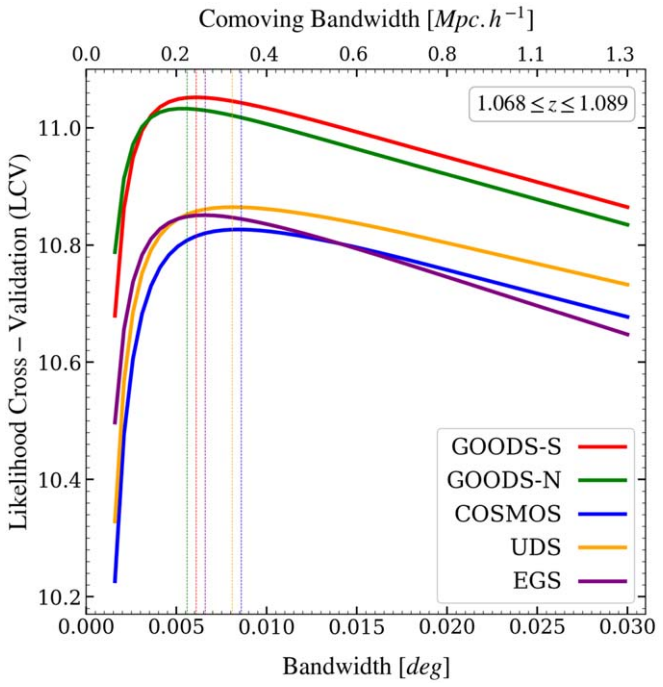

Figure 3. An example of the likelihood cross-validation optimization procedure at a given z-slice: $1.068 \leqslant z \leqslant 1.089$. We perform a grid search in the range $0.^{\circ}0001 \leqslant$ bandwidth $\leqslant 0.^{\circ}03$ with 50 steps to maximize the LCV and find the best bandwidth (b). The dashed vertical lines show optimized bandwidths at $z \sim 1$.

the local bandwidth (b_i) as (Abramson 1982)

$$b_i = b\left\{\frac{\sigma(\boldsymbol{X}_i)}{g}\right\}^{-\alpha} \tag{6}$$

where

$$\log g = \frac{1}{N}\sum_{i=1}^{N}\log \sigma(\boldsymbol{X}_i).$$

The sensitivity parameter, α, is a constant that satisfies $0 \leqslant \alpha \leqslant 1$ and can be fixed by simulation. In this study, we take a simple case where $\alpha = 0.5$ because the sensitivity parameter does not have a significant effect in wKDE measurement (Wang & Wang 2007). For each redshift slice, first, we estimate the bandwidth using the cross-validation method and then we employ the adaptive bandwidth technique (Equation (6)) to reduce the variance/bias in the estimation. Finally, we need to correct the density field for the boundary effect, which is explained in the following section.

3.4. Boundary Correction

The Kernel density estimation method assumes that the density field exists in the entire space. This assumption is not valid in most cases where a survey has data only for a small area of the sky. The trade-off between the area and the depth translates into a small coverage in deep surveys (e.g., CANDELS). Missing parts of the sky not covered in the survey result in an underestimation of the density field near the edge of the survey. Different methods have been developed to remove this problem, known as the boundary effect, e.g., the reflection method (Schuster 1985), the boundary kernel method (Müller 1991), and the transformation method (Marron & Ruppert 1994). Here we use the renormalization method to correct for this boundary effect.

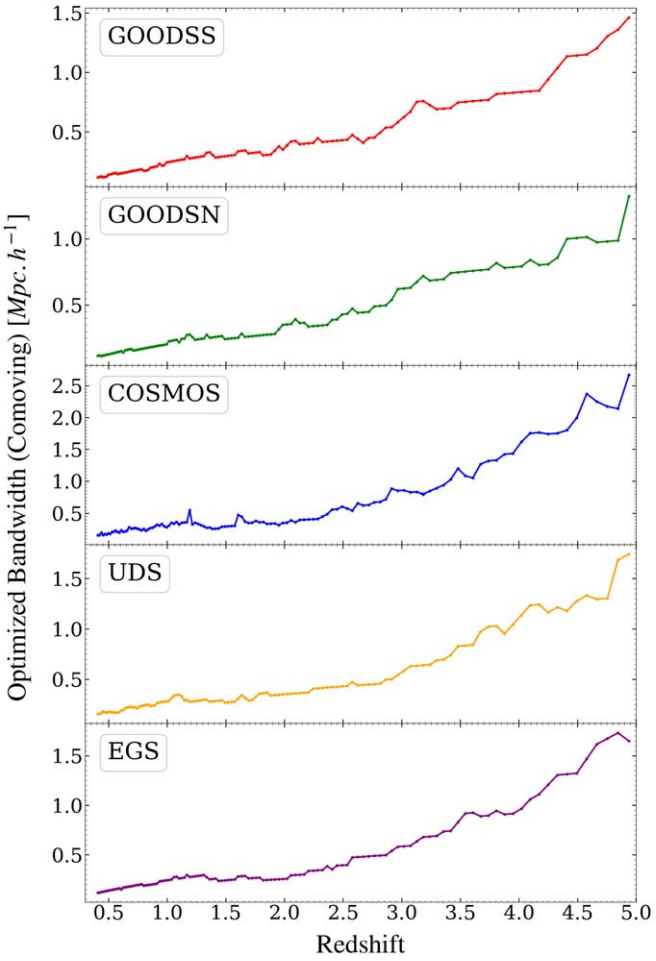

Figure 4. Optimized comoving global bandwidth (b) as a function of redshift for the five CANDELS fields. As we go to higher redshifts, we should increase the comoving size of the kernel function bandwidth to avoid the undesirable variance.

The first order of the expectation value of the density fields can be written as (Jones 1993)

$$\mathbb{E}(\sigma^j(\boldsymbol{X}_0)) \sim \sigma^j_{\rm True}(\boldsymbol{X}_0)\int_S \mathrm{K}(\boldsymbol{X}_i;\boldsymbol{X}_0) \tag{7}$$

where $\sigma^j_{\rm True}$ is the true underlying density field and the integration is performed over the survey area (S). Thus, a simple way to correct the boundary is to renormalize the density as

$$\sigma^j_{\rm corr}(\boldsymbol{X}_0) = \sigma^j(\boldsymbol{X}_0)n(\boldsymbol{X}_0) \tag{8}$$

where $n(\boldsymbol{X}_0)$ is the inverse of the kernel function integration centered at $\boldsymbol{X}_0$ over the survey area (S),

$$n^{-1}(\boldsymbol{X}_0) = \int_S \mathrm{K}(\boldsymbol{X}_i;\boldsymbol{X}_0) \tag{9}$$

This correction results in almost unbiased estimation of the density such that $\mathbb{E}(\sigma^j_{\rm corr}(\boldsymbol{X}_0)) \sim \sigma^j_{\rm True}(\boldsymbol{X}_0)$, but it may increase the variance close to the boundary.

Figure 5 shows the boundary correction coefficient (n) given the bandwidth of $0.^{\circ}0116$. At that bandwidth, 40% of galaxies are affected by boundary problem ($n > 1$), and it is crucial to

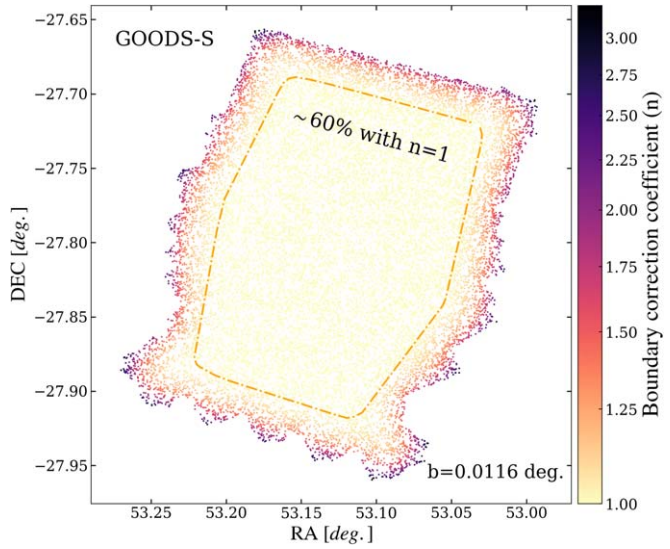

Figure 5. An example of the boundary correction coefficient (n) for galaxies in the GOODS-S field. It is shown that for the bandwidth of $0.^{\circ}0116$, the coefficient can be as large as ∼3.5. The orange dashed–dotted line encloses 60% of galaxies that are not affected by the boundary problem ($n = 1$).

apply a boundary correction to those galaxies. Not correcting for boundary effects can result in an underestimation by a factor of up to ∼3.5.

A common way to quantify the environment is by defining density contrast (δ) as

$$\delta = \frac{\sigma}{\bar{\sigma}} - 1 \tag{10}$$

where $\bar{\sigma}$ is the background number density, which can be evaluated using $\sum_i \omega_i^j / V$. Here, ω_i^j is the weight of the ith galaxy at the jth z-slice, and V is the volume of the corresponding z-slice. The boundary problem does not affect the background number density; however, it biases σ close to the edge of the survey. Thus, boundary correction is necessary to avoid missing overdensities close to the edge.

3.5. Catalogs and Density Maps

We utilize the boundary-corrected weighted von Mises kernel density estimation method to reconstruct the density field of galaxies at $0.4 \leqslant z \leqslant 5$ in the five CANDELS fields. Details of the density measurement technique have been explained in Sections 3.1–3.4 and are summarized below.

1. Divide the survey into redshift slices with a comoving width of $\sim 35\, h^{-1}$ Mpc (see Section 3.1).

   For each z-slice:
2. Weight the galaxies using their redshift PDFs to construct the two-dimensional weighted maps (see Section 3).
3. Perform a grid search on the bandwidth space to minimize the LCV function and find the optimum bandwidths (see Section 3.3).
4. Compute the density field associated with each galaxy using weighted KDE with the constant bandwidth drawn from the previous step (see Section 3.2) and apply the boundary correction technique (see Section 3.4).
5. Make the bandwidth adaptive based on the boundary-corrected densities (see Section 3.3) and rerun the weighted KDE with the adaptive bandwidths. Then, reapply the boundary correction method to the adaptively derived densities.

   The last step is to combine all z-slices to extract the density field associated with each galaxy.
6. For each galaxy, calculate the weighted summation of its density in all z-slices (see Section 3) to obtain the density field of the galaxy.

The full density field catalogs are available in the electronic version. Table 2 shows examples of the density measurements. The first four columns show the CANDELS ID, R.A., decl. and redshift ($z_{\rm best}$). The last three columns give the environmental properties, i.e., comoving/physical density and density contrast. Comoving density is the number of galaxies in a cube with a comoving volume of $1\, h^{-3}\,{\rm Mpc}^3$. The physical density can be computed by scaling the comoving density by a factor of $(1+z)^3$. The density contrast indicates the number density enhancement with respect to the average density in the vicinity of the galaxy (Equation (10)).

The comoving number density and density contrast of galaxies as a function of their redshifts are shown in Figure 10 in Appendix B. The limiting magnitude of the survey restricts the sources to a certain stellar mass range. Hence, the evolution of the comoving number density with redshift is an inevitable result of missing low-mass galaxies at higher redshifts. In contrast, we find that the average density contrast is almost constant with redshift. This implies that the stellar mass function for a total sample of quiescent and star-forming galaxies does not change significantly with the environment. Davidzon et al. (2016) have studied the effect of the environment on the shape of the galaxy stellar mass function up to redshift $z = 0.9$, finding that the environmental dependence of the stellar mass function becomes weaker with redshift.

The histogram of the density contrast is also shown for each field in Figure 10. For all the fields, we find a similar distribution of density contrast, which has a dynamic range of ∼10. For the entire sample of galaxies in all CANDELS fields, the average density contrast is 0.45 with a standard deviation of 0.75. This suggests that galaxies with a density contrast $\gtrsim$1.2 are located in an overdense region and those with density contrast $\lesssim -0.3$ reside in a void.

Using the technique described in this paper, we estimate the density maps for all the five CANDELS fields. The evolution of the large-scale structures is provided by 124 density maps covering $0.4 \leqslant z \leqslant 5$. The full density maps are available in the electronic version, with a few examples shown in Appendix A (Figure 9). In the density maps, we limited the range of the color bar to 5 to get a better contrast. Therefore, any density contrast above 5 is saturated with a dark red color.

4. Results

In this section, we use the estimated density fields to study the environmental effect on star formation activity of galaxies as a function of redshift. Here, we rely on the combined data from five widely separated fields to alleviate the effect of cosmic variance as well as the sample size.

4.1. Environmental Dependence of SFR and sSFR

We investigate the dependence of SFR and sSFR on the local overdensity. We build a mass-complete sample of galaxies in

Table 2
Density Field Measurements in the GOODS-S Field (Full Catalogs are Published in the Electronic Edition)

ID	R.A. (deg)	Decl. (deg)	Redshift	Comoving Density (h^3 Mpc^{-3})	Physical Density (h^3 Mpc^{-3})	Density Contrast
13889	53.1846685	−27.7875097	4.444	0.0112	1.7927	3.5429
13890	53.1610507	−27.7883341	1.095	0.1478	1.3476	1.7321
13893	53.1540231	−27.7876987	1.782	0.0569	1.2397	1.0454
13894	53.021758	−27.7874826	4.878	0.0099	2.0489	7.0415
13895	53.1157124	−27.7876168	1.187	0.0564	0.6183	0.269
13896	53.0802905	−27.7874276	2.407	0.0194	0.7487	0.0688
13902	53.1743111	−27.7876836	2.058	0.0223	0.6278	−0.138
13903	53.0335614	−27.7880437	1.083	0.0781	0.6991	0.4059
13911	53.1471765	−27.7884795	0.631	0.1096	0.4745	−0.2466
13912	53.1491844	−27.7878595	1.805	0.0553	1.2311	0.9543

(This table is available in its entirety in machine-readable form.)

four redshift intervals. Each interval contains galaxies with stellar mass greater than the completeness limit at that redshift. For example, the sample at $0.4 \leqslant z < 0.8$ consists of 6299 galaxies with $M \geqslant M_{\rm min}(0.8)$ where $M_{\rm min}(0.8)$ is the stellar mass completeness limit at $z = 0.8$. The properties of the sample are summarized in Table 3. Although we have density measurements up to $z = 5$, we limit our investigation to $z \leqslant 3.5$. A mass-complete sample of galaxies at $3.5 < z \leqslant 5$ suffers from a small sample size (<100) and may not be used to draw any statistically significant conclusions.

Figure 6 demonstrates the average SFR and sSFR as a function of density contrast in the four redshift intervals. It shows a clear anticorrelation between sSFR and environmental density. The same trend can be seen in the SFR–density relation. At low redshift, $0.4 \leqslant z < 0.8$, SFR decreases by a factor of ∼50 as the density contrast increases from $\delta \sim -0.5$ to $\delta \sim 6$. This drop is steeper (by an order of magnitude) for the sSFR. At $0.8 \leqslant z < 1.2$, we find similar anticorrelation. These trends are in full agreement with previous studies (e.g., Patel et al. 2009; Scoville et al. 2013; Darvish et al. 2016).

At high redshift, $1.2 \leqslant z < 2.2$, we find that both SFR–density and sSFR–density relations follow the same trends we observe at intermediate and low redshifts ($z < 1.2$). The average SFR and sSFR of galaxies in dense environments are significantly lower than those of galaxies residing in underdense regions. For example, the average sSFR decreases ∼1.3 dex with ∼1 dex increase in density contrast. Several studies revealed the persistence of the environmental quenching at high redshifts out to $z \sim 2$ (e.g., Grützbauch et al. 2012; Lin et al. 2012; Fossati et al. 2017; Guo et al. 2017; Kawinwanichakij et al. 2017; Ji et al. 2018). Our results confirm that anticorrelation exists in both SFR–density and sSFR–density relations at least out to $z \sim 2.2$.

Figure 6 also shows that the environment does play a significant role for the highest redshift bin, $2.2 \leqslant z < 3.5$. SFR–density and sSFR–density relations behave in the same way that we observe in the local universe. However, results need to be interpreted with caution since trends are found in different stellar mass ranges. For example, anticorrelation seen at $0.4 \leqslant z < 0.8$ corresponds to the galaxies with $\log(M/M_\odot) > 8.65$, while the relation at $2.2 \leqslant z < 3.5$ includes only massive galaxies with $\log(M/M_\odot) > 10.3$. The well-known relation between stellar mass and SFR in galaxies as a function of redshift confirms that the stellar mass plays a vital role in the star formation activity of galaxies (e.g., Peng et al. 2010). It suggests that star formation activity might be affected by both the local environment and stellar mass. Therefore, we disentangle the influence of environment and stellar mass in the next section before proceeding to the physical interpretation of the results.

Table 3
Properties of the Mass-complete Sample

Redshift Range	$\log(M_{\rm min}/M_\odot)$	Sample Size
$0.4 \leqslant z < 0.8$	8.65	6299
$0.8 \leqslant z < 1.2$	8.98	6279
$1.2 \leqslant z < 2.2$	9.67	6168
$2.2 \leqslant z \leqslant 3.5$	10.30	1047

4.2. SFR–Environment/Stellar Mass relation

Figure 7 presents the average SFR as a function of stellar mass and environment for the overall population of galaxies in the four redshift intervals. Colors indicate the average SFR in bins of environment and stellar mass. White areas show the regions with an inadequate number of data points (<20).

We find that the SFR of massive galaxies ($M \geqslant 10^{11}\,M_\odot$) is inversely correlated with the environment at all redshifts ($0.4 \leqslant z < 3.5$). For instance, at $1.2 \leqslant z < 2.2$, massive galaxies in dense environments on average form their stars ∼6 times more slowly than galaxies with the same stellar mass located in underdense regions. In contrast, we do not find significant environmental dependence on SFR of galaxies with lower stellar masses ($M < 10^{11}\,M_\odot$) at high redshifts ($1.2 \leqslant z < 3.5$). This reveals that the environmental quenching for very massive galaxies persists out to $z \sim 3.5$. This concurs well with the work done by Kawinwanichakij et al. (2017), which is conducted out to $z = 2$. Moreover, Figure 7 demonstrates strong evidence of environmental quenching for low-mass galaxies ($10^{9.5}\,M_\odot < M < 10^{11}\,M_\odot$) at $z < 1.2$ while this is not the case at higher redshifts ($z > 1.2$).

We also investigate the fraction of quiescent galaxies as a function of stellar mass and environment. Similar to Figure 7, we find evidence of both stellar mass and environmental quenching out to $z \sim 3.5$, such that the fraction of quiescent galaxies increases with increasing density contrast and stellar mass. In order to quantify the efficiency of environment and stellar mass in galactic quenching, we adopt the method introduced by Peng et al. (2010). We define environmental quenching efficiency, $\varepsilon_{\rm env}$, as the deficiency in the fraction of star-forming galaxies in the environment with overdensity δ

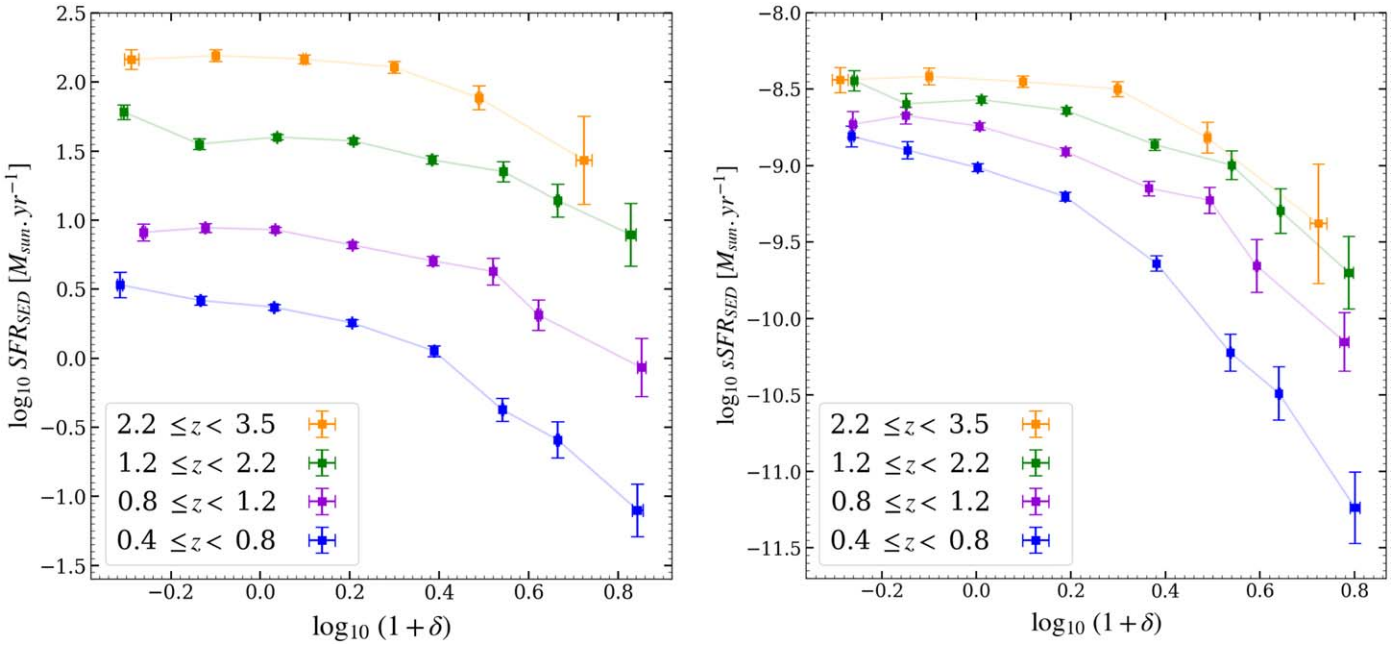

Figure 6. Environmental dependence of SFR and sSFR for a mass-complete sample of galaxies (Table 3) in four redshift bins spanning the redshift range $z = 0.4$–3.5. The average SFR and sSFR of galaxies in density contrast bins are plotted as a function of overdensity $(1 + \delta)$. Error bars show the statistical uncertainty of the average values.

compared to the underdense region:

$$\varepsilon_{\rm env}(\delta,\ \delta_0,\ M,\ z) = 1 - \frac{{\rm f_s}(\delta,\ M,\ z)}{{\rm f_s}(\delta_0,\ M,\ z)} \tag{11}$$

where $f_s(\delta,\ M,\ z)$ is the fraction of star-forming galaxies with stellar mass M that are located in an overdensity δ. δ_0 is the density contrast of the underdense environment. Following Kawinwanichakij et al. (2017), we consider the lowest 25% of the δ distribution (δ_{25}) as an underdense environment (δ_0) and we compute environmental quenching efficiency for galaxies that are located in an overdensity with δ greater than the 75th percentile of the δ distribution (δ_{75}). A similar quantity can be defined for mass quenching efficiency, $\varepsilon_{\rm mass}$,

$$\varepsilon_{\rm mass}(\delta,\ M,\ M_0,\ z) = 1 - \frac{f_{\rm s}(\delta,\ M,\ z)}{f_{\rm s}(\delta,\ M_0,\ z)} \tag{12}$$

where M_0 is the lowest stellar mass at any given redshift (z), which can be obtained from the stellar mass completeness limit ($M_{\rm min}(z)$). We compute mass quenching efficiency for galaxies with $\delta < \delta_{75}$.

In order to calculate the fraction of star-forming galaxies, we separate star-forming and quiescent galaxies based on their rest-frame U, V, and J colors along with the criteria of Muzzin et al. (2013).

The stellar mass dependence of the mass quenching efficiency, $\varepsilon_{\rm mass}(\delta < \delta_{75},\ M,\ M_{\rm min}(z),\ z)$ and environmental quenching efficiency, $\varepsilon_{\rm env}(\delta > \delta_{75},\ \delta < \delta_{25},\ M,\ z)$ are shown in Figure 8. The efficiencies are calculated in stellar mass bins, $\Delta M \sim 0.5$ dex, and error bars (shaded regions) are obtained considering the Poisson statistics for the number of quiescent/star-forming galaxies.

At all redshifts, mass quenching efficiency increases significantly with stellar mass, which is consistent with previous works (e.g., Peng et al. 2010). We also find that the environmental quenching efficiency is not independent of the stellar mass and it clearly increases with it, although this rise is weaker than that of the mass quenching efficiency (see also Lin et al. 2014; Papovich et al. 2018). At $z < 1.2$, the environmental quenching is dominant for low-mass galaxies ($M \lesssim 10^{10}\,M_{\odot}$). For example, at $0.4 \leqslant z < 0.8$, the environmental quenching is $\sim$10 times stronger than the mass quenching. For massive galaxies ($M \gtrsim 10^{10}\,M_{\odot}$), mass quenching is the dominant quenching mechanism at all redshifts; however, environmental quenching is significant for the most massive galaxies ($M \gtrsim 10^{11}\,M_{\odot}$). For instance, at $2.2 \leqslant z < 3.5$, the environment and the stellar mass are almost equally responsible for the quenching of very massive galaxies ($\varepsilon_{\rm mass} \sim \varepsilon_{\rm env}$). This result reinforces our previous findings in Figure 7 that environmental quenching of very massive galaxies exists at least out to $z \sim 3.5$. It also confirms that environmental quenching is efficient for low-mass galaxies at low and intermediate redshifts ($z < 1.2$) (see also Peng et al. 2010; Quadri et al. 2012; Scoville et al. 2013; Lin et al. 2014; Lee et al. 2015; Darvish et al. 2016; Nantais et al. 2016; Guo et al. 2017; Fossati et al. 2017; Kawinwanichakij et al. 2017; Ji et al. 2018).

4.3. Origin of the Environmental Quenching

Although most studies, including this work, found strong evidence of environmental quenching out to high redshifts, the physical mechanisms that are responsible are not clearly understood. van de Voort et al. (2017) found a suppression of the cool gas accretion rate in dense environments at all redshifts, which becomes stronger at lower redshifts. This implies that a dense environment prevents the accretion of cold gas into the galaxy (cosmological starvation). As a result, the galaxy starts to consume the remaining gas reservoir in the depletion timescale, $t_{\rm depl} \propto M_{\rm gas}/{\rm SFR}$. This scenario is known as the "overconsumption" model (McGee et al. 2014; Balogh et al. 2016) and implies that the depletion time ($t_{\rm depl}$) depends on both stellar mass and redshift. The model predicts a short

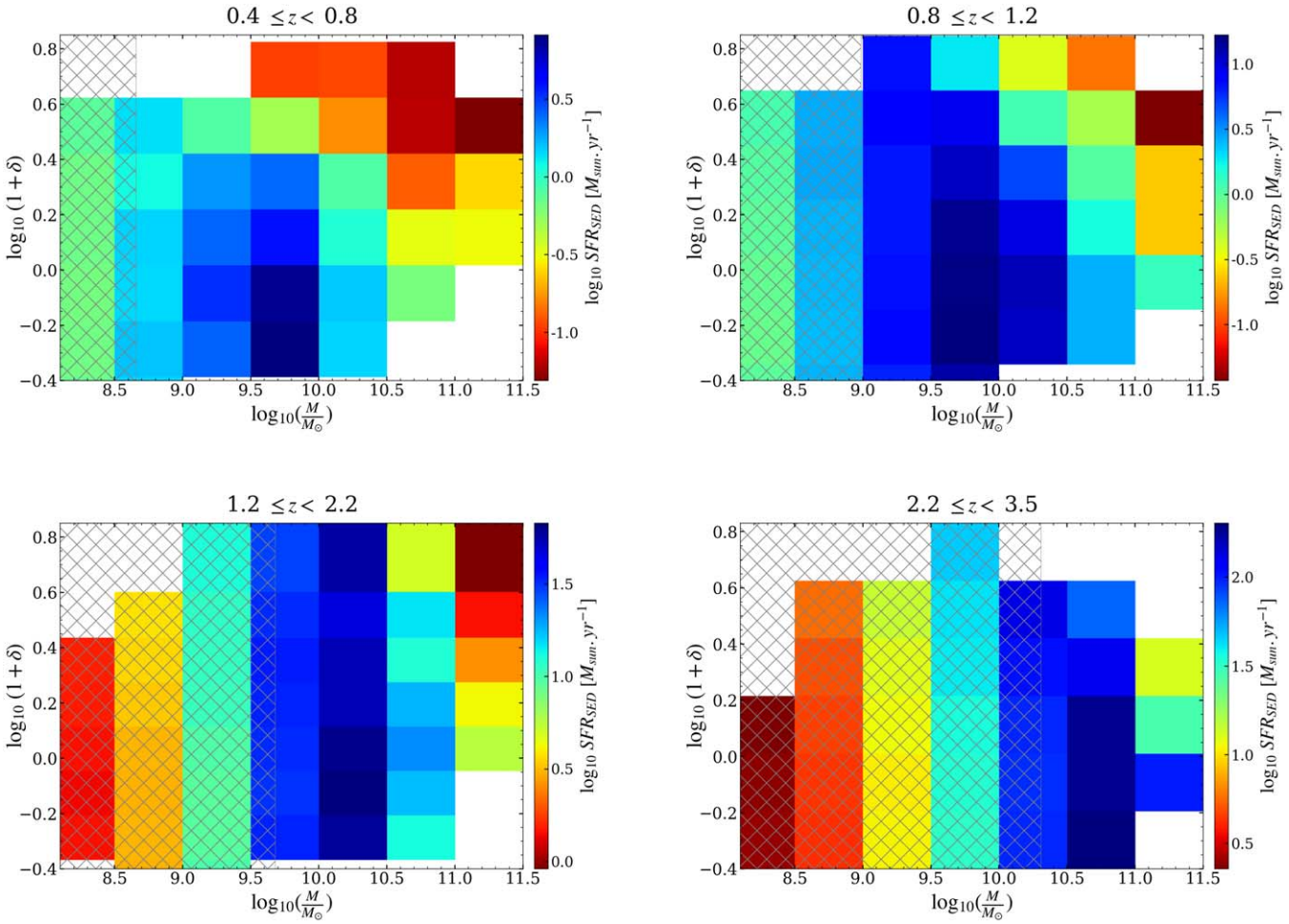

Figure 7. Average star formation rate in the bins of stellar mass and environment in four redshift intervals. The gray shaded regions show the incomplete stellar mass ranges. At all redshifts, we observe both environmental quenching and mass quenching for massive galaxies. We also find strong evidence of environmental quenching for low-mass galaxies at low redshift.

depletion timescale (<100 Myr) for massive galaxies at high redshift. Therefore, an "overconsumption" scenario could explain the environmental quenching that we observe here for massive galaxies at high redshifts (Kawinwanichakij et al. 2017). Feldmann & Mayer (2015) also showed through their simulation that, at $z \sim 3.5$, the sSFR of a massive galaxy ($M \sim 10^{11}\,M_{\odot}$) drops by almost an order of magnitude within a few hundred million years. They found that this sudden halt at $z \sim 3.5$ is not caused by feedback processes and happens primarily due to the termination of the cool gas accretion. This provides further support for the idea that massive galaxies become quenched abruptly when their fresh gas accretion is terminated, possibly by being located in a dense environment. In addition, the lack of environmental quenching of low-mass galaxies at high redshift can be explained by their low SFR, which results in a longer depletion time (Balogh et al. 2016; Kawinwanichakij et al. 2017).

Furthermore, the "overconsumption" model could explain our observations at low redshift (down to $z \sim 0.4$). For galaxies with stellar mass $M \sim 10^{10.5}\,M_{\odot}$, the depletion time ($t_{\rm depl}$) increases with decreasing redshift and reaches ~2 Gyr at $z \sim 0.4$ (McGee et al. 2014), which is shorter than the typical dynamical timescale at that redshift ($t_{\rm dyn} \sim 4$ Gyr) (Balogh et al. 2016; Foltz et al. 2018). This implies that the dynamical gas stripping processes are not required to explain our observation at low redshift. Moreover, the evolution of environmental quenching efficiency with stellar mass supports the "overconsumption" model where the depletion time is longer for low-mass galaxies, resulting in weaker quenching efficiency. Therefore, the "overconsumption" picture is most likely the dominant mechanism of environmental quenching, at least in the redshift range of this study. However, it is worth highlighting that the depletion time grows fast in the local universe, such that it reaches >10 Gyr at $z = 0$ for galaxies with intermediate stellar masses ($M \sim 10^{10.5}\,M_{\odot}$). This is longer than the dynamical timescale (Balogh et al. 2016). Consequently, "overconsumption" is likely not an effective quenching pathway in the local universe and other dynamical processes are needed to explain the strong environmental quenching observed at $z \sim 0$ (Peng et al. 2010).

5. Discussion

In this work, we introduce a robust method for reconstructing the underlying number density field of galaxies. The performance of KDE has been well explored by statisticians. They found that KDE can precisely estimate underlying densities of any shape, provided that the bandwidth is selected appropriately (e.g., Silverman 1986). We adopt a well-known LCV method to find the optimized bandwidth (e.g., Hall 1982). Alternatively, one can use least-squares cross-validation

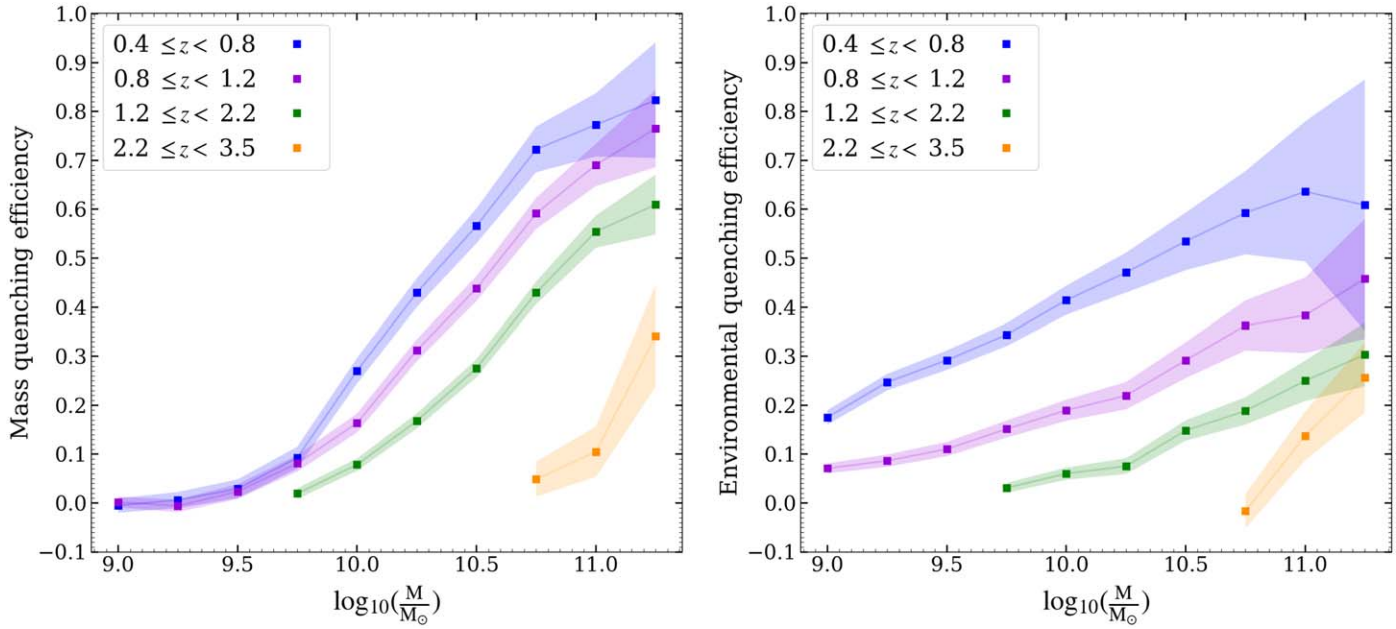

Figure 8. The mass quenching efficiency and environmental quenching efficiency, $\varepsilon_{\rm env}(\delta > \delta_{75}, \delta < \delta_{25}, M)$ as a function of stellar mass. The efficiencies are calculated in stellar mass bins, $\Delta M \sim 0.5$ dex. Shaded regions show the uncertainty of efficiencies considering the Poisson statistics for the number of quiescent/star-forming galaxies.

(LSCV) (Bowman 1984), which is based on minimizing the integrated square error between the estimated and true densities. The LSCV method of bandwidth selection suffers the disadvantage of high variability (Jones et al. 1996) and a tendency to undersmooth (Chiu 1991). We also correct densities for a systematic bias (underestimation) near the edge of the survey using renormalization. This assumes a symmetric galaxy distribution with respect to boundaries near the edges and may cause misestimated densities. This inevitable issue can be eliminated by observing as deep as CANDELS over a wider area.

Fossati et al. (2017) have measured the environmental density for a $JH_{140} \leqslant 24$ sample of 18,745 galaxies in the 3D-*HST* survey (Skelton et al. 2014) from $z = 0.5$ to 3, adopting the circular aperture method (aperture radius fixed at 0.75 Mpc and width of z-slices at $\Delta v = 1500\,{\rm km\ s^{-1}}$). We find a significant difference between their density contrasts and our measurements. Fossati et al. (2017) did not use the uniformly calculated probability distributions of photometric redshifts. Instead, they assign redshifts based on a nearby galaxy with a spectroscopic redshift. They also use public data from a wider field for edge correction. We adopt the renormalization method for edge correction since we use the widest homogeneous fields with a depth of F160w = 26 AB mag.

We explore any trends that may exist between the estimated densities and redshift in Figure 10. This ensures that the average density contrast does not evolve strongly with redshift. Otherwise, the diagram of any physical parameter (e.g., SFR, sSFR, or quiescent fraction) as a function of density contrast would not be informative about the role of the environment, and trends could be affected by redshift evolution of physical parameters.

Furthermore, the possibility of unrealistic trends due to the different assumptions in SED fitting (e.g., star formation history) also needs to be investigated. As a test case, we repeat our analysis based on the SED fitting method of Pacifici et al. (2012), which provides a library of SEDs assuming star formation histories from a semi-analytical model. Although the trends in Figure 6 are more sensitive to SED fitting priors, the stellar mass dependence of environmental quenching efficiency (Figure 8) does not change with new measurements. This reassures us that the present evidence of environmental quenching at high redshift and the evolution of environmental quenching efficiency with stellar mass are not affected by SED fitting priors (Section 2), especially by exponentially declining star formation history.

6. Summary

In this work, we report measurements of the environment for an F160w $\leqslant$ 26 AB mag sample of 86,716 galaxies in the five CANDELS fields (GOODS-South, GOODS-North, COSMOS, EGS, UDS) at $0.4 \leqslant z \leqslant 5$. We introduce a new method, boundary-corrected weighted von Mises kernel density estimation, to reconstruct the underlying density field of galaxies. We find the optimal bandwidth for the von Mises kernel function in 124 z-slices spanning from $z = 0.4$ to 5 using the LCV method. This allows us to create density field maps with the lowest bias/variance.

We then use the density measurements to investigate the role of the environment in star formation activity of a mass-complete sample of galaxies at $0.4 \leqslant z \leqslant 3.5$. Our findings are summarized as follows.

1. At all redshifts, the average SFR and sSFR for a mass-complete sample of galaxies decrease with increasing density contrast. The trend is steeper at low redshift ($0.4 \leqslant z < 0.8$) such that the average SFR decreases by a factor of $\sim$50 as the density contrast increases from $\delta \sim -0.5$ to $\delta \sim 6$.
2. We find strong evidence of environmental quenching for massive galaxies ($M \gtrsim 10^{11}\,M_{\odot}$) out to $z \sim 3.5$. We measured that the environmental quenching efficiency is $\gtrsim$0.2, implying that a dense environment has $\gtrsim$20% more massive quiescent galaxies than an underdense region.

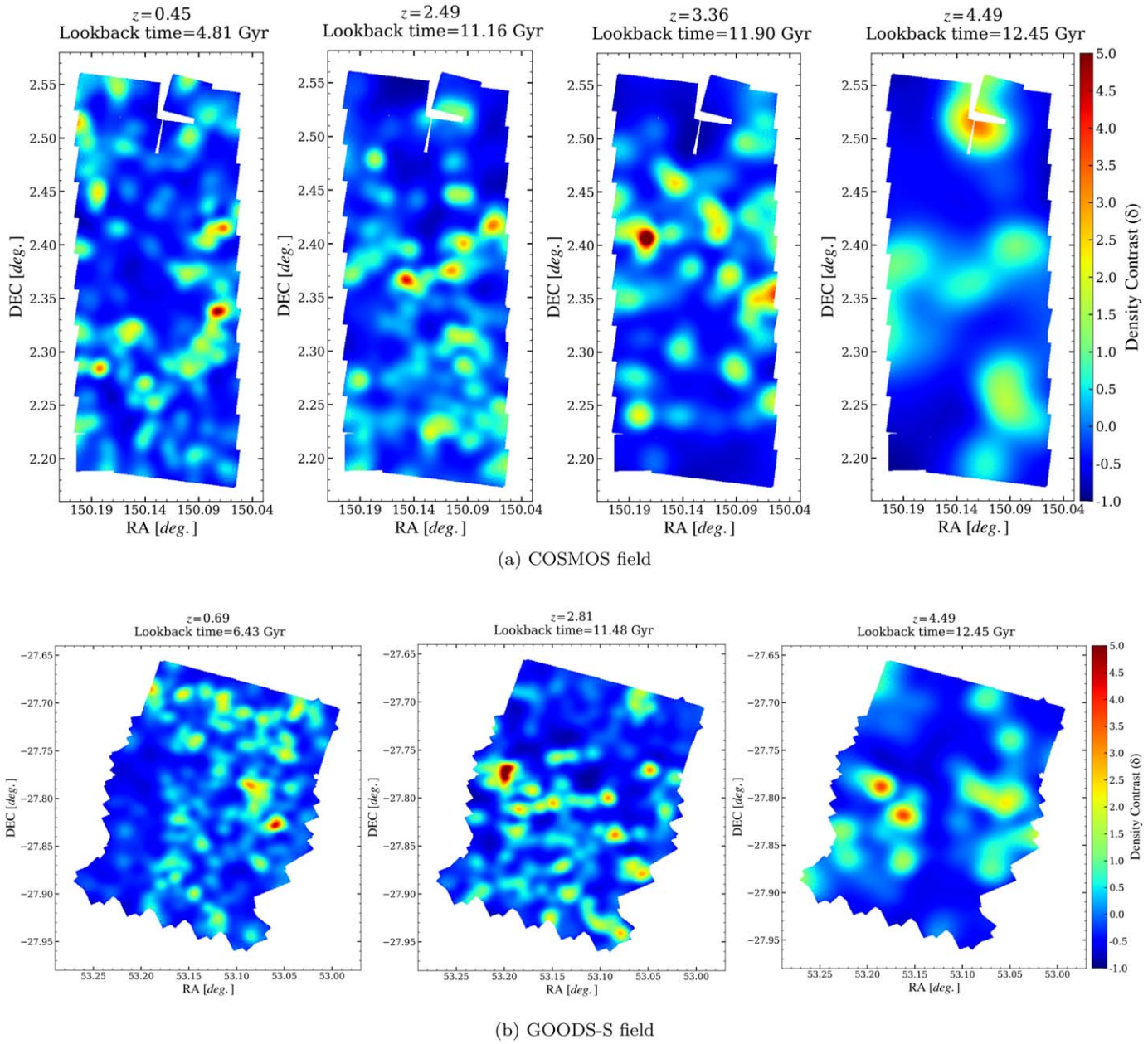

Figure 9. Density maps. Plots for the 124 redshift slices are available in an animated format in the online version.
(An animation of this figure is available.)

This ratio reaches ∼60% for the lowest redshift bin of this study ($0.4 \leqslant z < 0.8$).

3. We find that the environmental quenching efficiency increases with stellar mass. This observation supports the "overconsumption" model for environmental quenching, where gas depletion happens once fresh gas accretion stops due to a dense environment. The gas depletion time depends on stellar mass and redshift and could explain the stellar mass dependence of the environmental quenching efficiency. The depletion time becomes longer (>10 Gyr) at lower redshifts, so it could not be a proper quenching pathway in the local universe; however, "overconsumption" is most likely the dominant environmental quenching mechanism in the redshift range of this study.

We thank the anonymous referee for providing insightful comments and suggestions that improved the quality of this work. We would like to acknowledge the contribution of Adriano Fontana, Janine Pforr, Mara Salvato, Tommy Wiklind, and Stijn Wuyts to the updated version of the photometric redshift catalog. N.C. would like to thank Ali Ahmad Khostovan for useful suggestions and discussions.

Appendix A
Density Maps

We release overdensity maps of 124 z-slices ranging from $z = 0.4$ to 5 for all CANDELS fields. A few examples are provided in Figure 9, but the full set of plots for the 124 z-slices are available in animation in the electronic

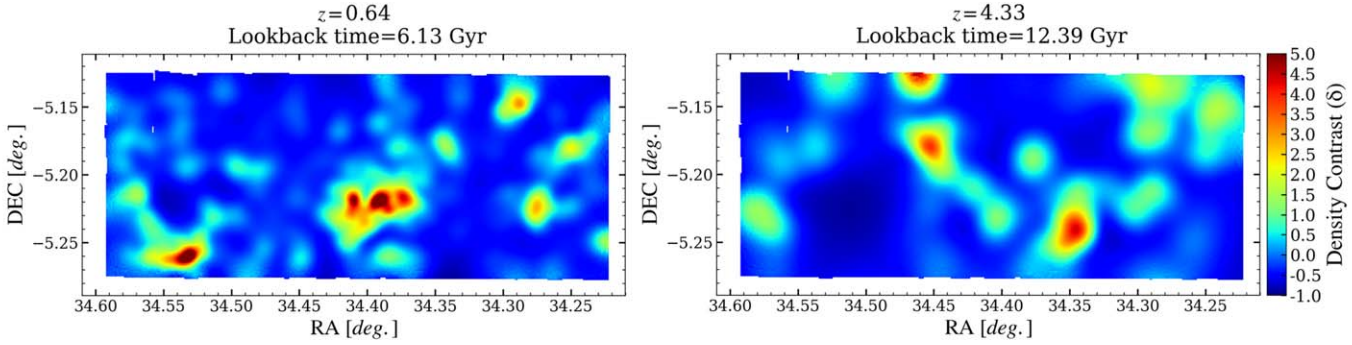

(c) UDS field

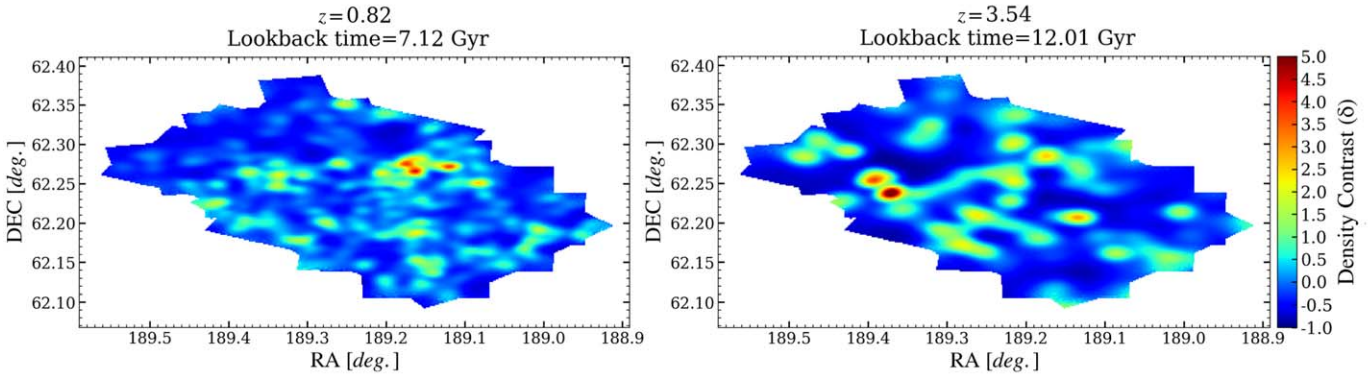

(d) GOODS-N field

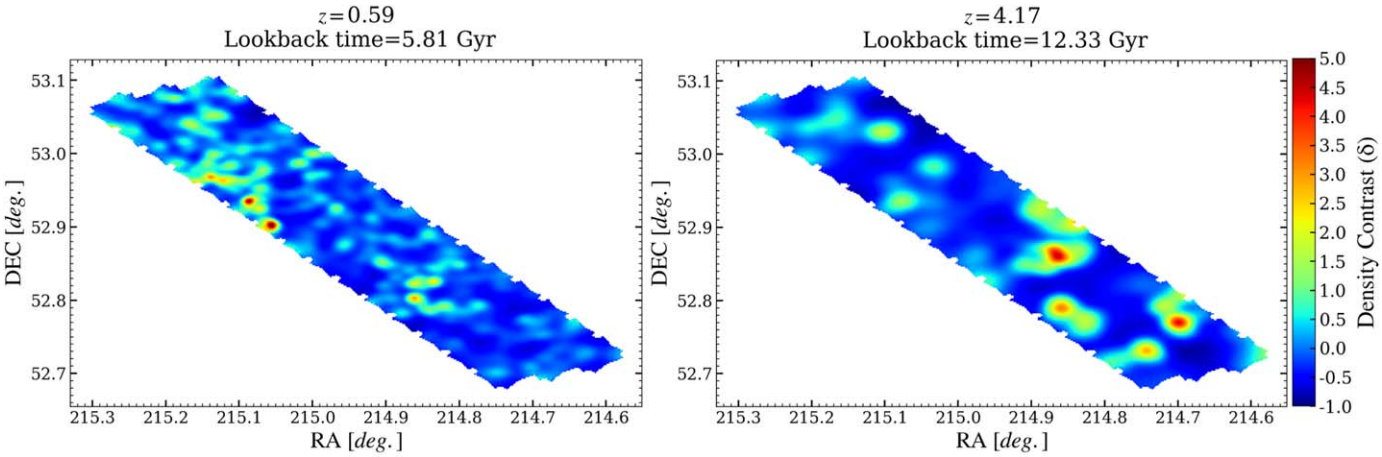

(e) EGS field

Figure 9. (Continued.)

version. In density maps, the range of the color bar is limited to 5 to get a better contrast. As we expect, structures on the fields with a higher decl. (e.g., GOODS-N and EGS) are elongated along the R.A. axis, which is the natural effect of mapping on (R.A., decl.) coordinates. It should be recalled that the density contrast of a galaxy is inferred from multiple density maps (z-slices) considering its contribution in each z-slice, which is determined by the photo-z PDF.

Appendix B
Redshift Evolution of Density Measurements

In this section, we investigate the correlation between density measurements and redshift. Figure 10 shows the comoving number density and the density contrast as a function of redshift along with the distribution of density contrast separately for each field. Despite the clear evolution of comoving number density, the average density contrast, $\langle 1 + \delta \rangle$, is almost constant with redshift. Although we find

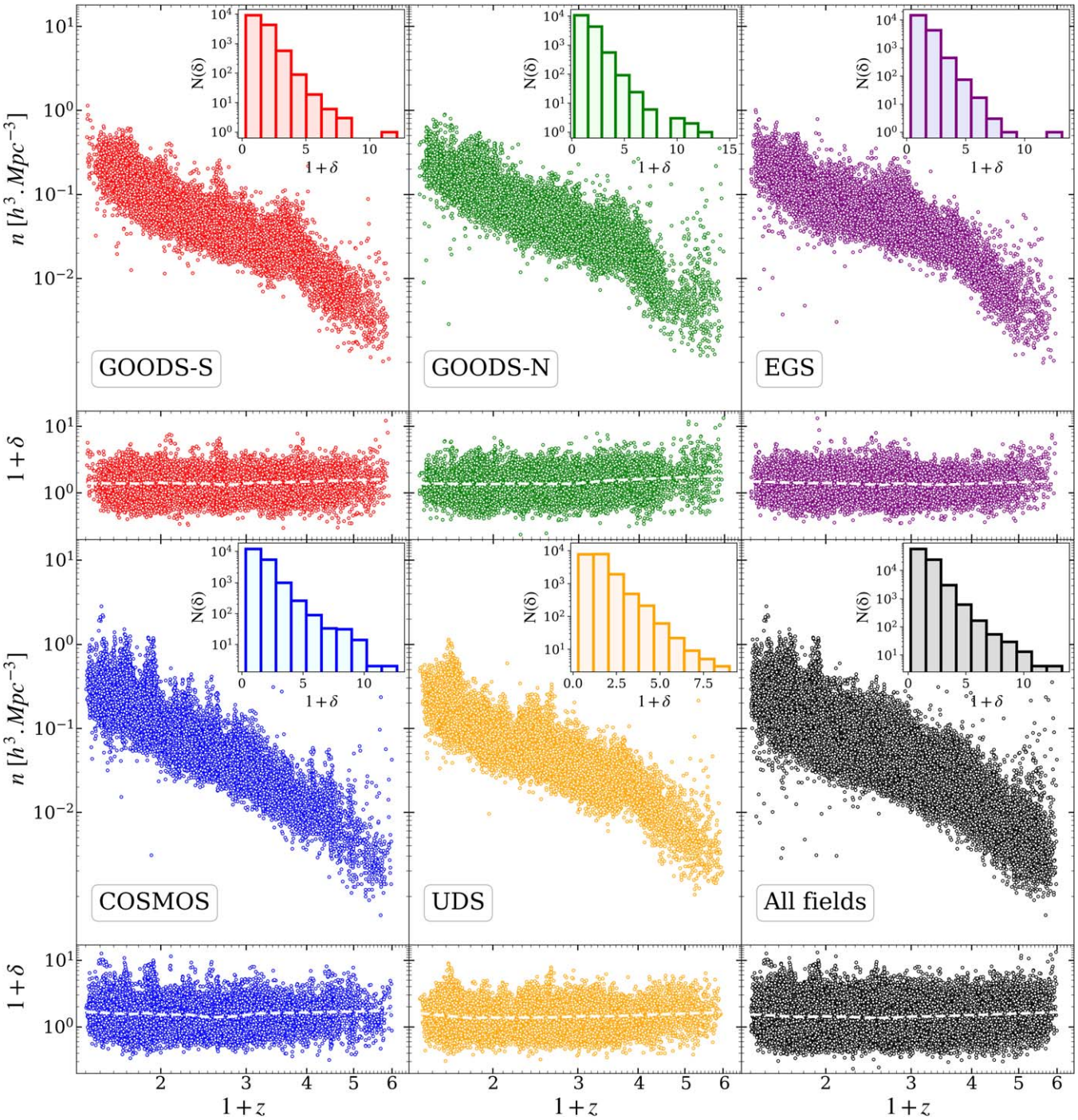

Figure 10. The comoving number density and the density contrast as a function of redshift as well as the histogram of density contrast for each field. The comoving number density decreases with redshift due to the magnitude limit of the survey, while the average density contrast (white dashed lines) is almost constant over cosmic time. This can be explained by the weak dependence of the stellar mass function on the environment. For all the fields, we find a similar distribution of density contrast, which has a dynamic range of ∼10.

modest evidence of systematic trends between $\langle 1+\delta \rangle$ and redshift, especially at $z \gtrsim 3$, the variation of $\langle 1+\delta \rangle$ with redshift is limited to $\lesssim$0.3. Thus, the study of the physical properties of galaxies (e.g., SFR) versus density contrast (Section 4) is not affected by the redshift evolution of overdensity measurements. We note that the average of $1+\delta$ is slightly higher than one since we do not define the density of the background ($\bar{\sigma}$ in Equation (10)) as the average density of galaxies. We define background density as the number of galaxies (computed from their photo-z PDFs) within each z-slice divided by the volume of that z-slice.

ORCID iDs

Nima Chartab https://orcid.org/0000-0003-3691-937X
Behnam Darvish https://orcid.org/0000-0003-4919-9017
Steve Finkelstein https://orcid.org/0000-0001-8519-1130
Yicheng Guo https://orcid.org/0000-0003-2775-2002
Kyoung-Soo Lee https://orcid.org/0000-0003-3004-9596

Jeffrey A. Newman https://orcid.org/0000-0001-8684-2222
Camilla Pacifici https://orcid.org/0000-0003-4196-0617
Casey Papovich https://orcid.org/0000-0001-7503-8482
Zahra Sattari https://orcid.org/0000-0002-0364-1159
Abtin Shahidi https://orcid.org/0000-0001-6975-6293
Henry C. Ferguson https://orcid.org/0000-0001-7113-2738
Mauro Giavalisco https://orcid.org/0000-0002-7831-8751
Marziye Jafariyazani https://orcid.org/0000-0001-8019-6661

References

Abramson, I. S. 1982, AnSta, 10, 1217
Alt, H., & Godau, M. 1995, Int. J. Comput. Geom. Appl., 5, 75
Arnouts, S., Cristiani, S., Moscardini, L., et al. 1999, MNRAS, 310, 540
Balogh, M., Eke, V., Miller, C., et al. 2004, MNRAS, 348, 1355
Balogh, M. L., McGee, S. L., Mok, A., et al. 2016, MNRAS, 456, 4364
Barro, G., Pérez-González, P. G., Cava, A., et al. 2019, ApJS, 243, 22
Bowman, A. W. 1984, Biometrika, 71, 353
Bruzual, G., & Charlot, S. 2003, MNRAS, 344, 1000
Calzetti, D., Armus, L., Bohlin, R. C., et al. 2000, ApJ, 533, 682
Capak, P., Abraham, R. G., Ellis, R. S., et al. 2007, ApJS, 172, 284
Chabrier, G. 2003, PASP, 115, 763
Chiu, S.-T. 1991, AnSta, 19, 1883
Cooper, M. C., Newman, J. A., Weiner, B. J., et al. 2008, MNRAS, 383, 1058
Darvish, B., Mobasher, B., Sobral, D., et al. 2016, ApJ, 825, 113
Darvish, B., Mobasher, B., Sobral, D., Scoville, N., & Aragon-Calvo, M. 2015, ApJ, 805, 121
Davidzon, I., Cucciati, O., Bolzonella, M., et al. 2016, A&A, 586, A23
Dressler, A. 1980, ApJ, 236, 351
Elbaz, D., Daddi, E., Le Borgne, D., et al. 2007, A&A, 468, 33
Feldmann, R., & Mayer, L. 2015, MNRAS, 446, 1939
Foltz, R., Wilson, G., Muzzin, A., et al. 2018, ApJ, 866, 136
Fossati, M., Wilman, D. J., Mendel, J. T., et al. 2017, ApJ, 835, 153
Galametz, A., Grazian, A., Fontana, A., et al. 2013, ApJS, 206, 10
García-Portugués, E., Crujeiras, R. M., & González-Manteiga, W. 2013, J. Multivar. Anal., 121, 152
Grogin, N. A., Kocevski, D. D., Faber, S. M., et al. 2011, ApJS, 197, 35
Grützbauch, R., Bauer, A. E., Jørgensen, I., & Varela, J. 2012, MNRAS, 423, 3652
Grützbauch, R., Conselice, C. J., Bauer, A. E., et al. 2011, MNRAS, 418, 938
Guo, Y., Bell, E. F., Lu, Y., et al. 2017, ApJL, 841, L22
Guo, Y., Ferguson, H. C., Giavalisco, M., et al. 2013, ApJS, 207, 24
Hall, P. 1982, Biometrika, 69, 383
Ilbert, O., Arnouts, S., McCracken, H. J., et al. 2006, A&A, 457, 841
Ilbert, O., Capak, P., Salvato, M., et al. 2009, ApJ, 690, 1236
Ji, Z., Giavalisco, M., Williams, C. C., et al. 2018, ApJ, 862, 135
Jones, M. C. 1993, Stat. Comput., 3, 135
Jones, M. C., Marron, J. S., & Sheather, S. J. 1996, J. Am. Stat. Assoc., 91, 401
Kauffmann, G., White, S. D. M., Heckman, T. M., et al. 2004, MNRAS, 353, 713
Kawinwanichakij, L., Papovich, C., Quadri, R. F., et al. 2017, ApJ, 847, 134
Kennicutt, R. C., Jr. 1998, ARA&A, 36, 189
Koekemoer, A. M., Faber, S. M., Ferguson, H. C., et al. 2011, ApJS, 197, 36
Lee, S.-K., Im, M., Kim, J.-W., et al. 2015, ApJ, 810, 90
Lin, L., Dickinson, M., Jian, H.-Y., et al. 2012, ApJ, 756, 71
Lin, L., Jian, H.-Y., Foucaud, S., et al. 2014, ApJ, 782, 33
Marron, J. S., & Ruppert, D. 1994, J. R. Stat. Soc. Ser. B, 56, 653
McGee, S. L., Bower, R. G., & Balogh, M. L. 2014, MNRAS, 442, L105
Müller, H.-G. 1991, Biometrika, 78, 521
Muzzin, A., Marchesini, D., Stefanon, M., et al. 2013, ApJ, 777, 18
Muzzin, A., Wilson, G., Yee, H. K. C., et al. 2012, ApJ, 746, 188
Nantais, J. B., van der Burg, R. F. J., Lidman, C., et al. 2016, A&A, 592, A161
Nayyeri, H., Hemmati, S., Mobasher, B., et al. 2017, ApJS, 228, 7
Pacifici, C., Charlot, S., Blaizot, J., & Brinchmann, J. 2012, MNRAS, 421, 2002
Papovich, C., Kawinwanichakij, L., Quadri, R. F., et al. 2018, ApJ, 854, 30
Parzen, E. 1962, Ann. Math. Stat., 33, 1065
Patel, S. G., Holden, B. P., Kelson, D. D., Illingworth, G. D., & Franx, M. 2009, ApJL, 705, L67
Peng, Y.-j., Lilly, S. J., Kovač, K., et al. 2010, ApJ, 721, 193
Pozzetti, L., Bolzonella, M., Zucca, E., et al. 2010, A&A, 523, A13
Quadri, R. F., Williams, R. J., Franx, M., & Hildebrandt, H. 2012, ApJ, 744, 88
Schuster, E. F. 1985, Commun. Stat. Theory Meth., 14, 1123
Scoville, N., Arnouts, S., Aussel, H., et al. 2013, ApJS, 206, 3
Scoville, N., Aussel, H., Brusa, M., et al. 2007, ApJS, 172, 1
Silverman, B. W. 1986, Density Estimation for Statistics and Data Analysis (Berlin: Springer), 1
Skelton, R. E., Whitaker, K. E., Momcheva, I. G., et al. 2014, ApJS, 214, 24
Stefanon, M., Yan, H., Mobasher, B., et al. 2017, ApJS, 229, 32
van de Voort, F., Bahé, Y. M., Bower, R. G., et al. 2017, MNRAS, 466 3460
Wang, B., & Wang, X. 2007, arXiv:0709.1616
Woo, J., Dekel, A., Faber, S. M., et al. 2013, MNRAS, 428, 3306